Supporting Information:

Photoacoustic sensing of trapped fluids in nanoporous thin films: device engineering and sensing scheme

Giulio Benetti,[†,‡,¶] Marco Gandolfi,[†,‡,§] Margriet J Van Bael,[¶] Luca Gavioli,[†,‡] Claudio Giannetti,[†,‡] Claudia Caddeo,[‖] and Francesco Banfi[*,†,‡]

†*Interdisciplinary Laboratories for Advanced Materials Physics (I-LAMP), Università Cattolica del Sacro Cuore, Via Musei 41, 25121 Brescia, Italy*

‡*Dipartimento di Matematica e Fisica, Università Cattolica del Sacro Cuore, Via Musei 41, 25121 Brescia, Italy*

¶*Laboratory of Solid State Physics and Magnetism, Department of Physics and Astronomy, KU Leuven, Celestijnenlaan 200D, B-3001 Leuven, Belgium*

§*Laboratory for Soft Matter and Biophysics, Department of Physics and Astronomy, KU Leuven, Celestijnenlaan 200D, B-3001 Leuven, Belgium*

‖*Istituto Officina dei Materiali (CNR - IOM) Cagliari, Cittadella Universitaria, I-09042 Monserrato, Cagliari, Italy*

E-mail: francesco.banfi@unicatt.it

1 Device design details

1.1 MD details

The velocity-Verlet algorithm is used to solve the equations of motion. The Nosé-Hoover thermostat with relaxation time equal to 100 fs was used to control the simulation temperature. All the interactions were cut off at 0.8 nm. A possible choice to reduce the computational cost is to increase the timestep, provided that the calculated properties are unaffected and that the energy is conserved in microcanonical (NVE) runs. To this aim, we performed several simulations at increasing timesteps, followed by a NVE 1 ns long run. The final configuration and mass density were unaffected by the timestep size up to more than 10 fs, and energy was conserved during the NVE run. We thus set the timestep of all our simulations to 10 fs. Further information is available elsewhere.[1]

1.2 Filling Factor, Volume and Thickness

Formally the Filling Factor (FF) of the Ag NPs film is defined as the ratio between the volume occupied by the Ag NPs V_{NP} and the total volume of the film V (for a slab of non porous silver, $FF = 1$). The relation between the FF and the film porosity hence reads: porosity $= 1 - FF$.

The MD simulations are performed by shooting the NPs on a rectangular domain of size $L_x \times L_y$=35×20 nm^2. The z axis is perpendicular to this rectangular domain. The film thickness is calculated by reticulating the rectangular domain (serving as the sample base) into square cells of 0.5×0.5 nm^2. Each cell is indexed by a pair of integers (n_x, n_y), where $n_x \in \{1, 2, 3, ..70\}$ and $n_y \in \{1, 2, 3, ..40\}$. The z-coordinate of the top-most atom falling inside the cell (n_x, n_y) is $\tilde{z}(n_x, n_y)$. Averaging the latter quantity on all the available cells it is possible to obtain the average film thickness h. From the average thickness, the total number of deposited atoms N and the volume of the Ag primitive cell V_{1Ag}, the film filling

factor is retrieved as:

$$FF = \frac{V_{NP}}{V} = \frac{N\,V_{1Ag}}{h(L_x L_y)} \tag{S1}$$

1.3 Pore size

To quantify the pore size, we employed the method developed by Sainto and Toriwaki[2] and later optimised to study the trabecular bone structures.[2–4]

Briefly, the 3D void scaffold is partitioned in small cubic voxels (cube edge of 0.25 nm). For each voxel $\mathcal{V}$, the *punctual pore size* is defined as the diameter of the greatest sphere completely inscribed in the void scaffold and containing $\mathcal{V}$. By averaging the punctual pore size for all the potentially permeable empty voxels, we obtained the average pore size and its standard deviation.

2 Sensing scheme

2.1 Derivation of Eq.2 and its applicability

In this section we derive Equation 2 of the main text. We have already discussed in the main text that the contribution of the n-th breathing mode to the time-resolved optical trace is described by the expression:

$$F_n(t) = A_n e^{-t/\tau_n}\ \cos(2\pi f_n\, t + \phi_n)\ \theta(t). \tag{S2}$$

Now we perform Fourier's transform of $F_n(t)$:

$$\tilde{F_n}(f) = \int_{-\infty}^{+\infty} F_n(t) e^{-i(2\pi f)t} dt = A_n \int_0^{+\infty} e^{-t/\tau_n}\ \cos(2\pi f_n\, t + \phi_n) e^{-i(2\pi f)t} dt =$$

$$= \frac{A_n}{2}\left\{ e^{i\phi} \int_0^{+\infty} \exp\left[\left(-\frac{1}{\tau_n} + 2\pi i\,(f_n - f)\right) t\right] dt + e^{-i\phi} \int_0^{+\infty} \exp\left[\left(-\frac{1}{\tau_n} - 2\pi i\,(f_n + f)\right) t\right] dt \right\} =$$

$$= \frac{A_n}{2}\left\{ \frac{e^{i\phi}}{\frac{1}{\tau_n} + 2\pi i\,(f - f_n)} + \frac{e^{-i\phi}}{\frac{1}{\tau_n} + 2\pi i\,(f + f_n)} \right\} = A_n \frac{\left(\frac{1}{\tau_n} + 2\pi i f\right)\cos\phi - 2\pi f_n \sin\phi}{\left[4\pi^2(f_n^2 - f^2) + \frac{1}{\tau_n^2}\right] + 4\pi i \frac{f}{\tau_n}} \tag{S3}$$

As a consequence, the modulus of the Fourier's transform is:

$$\left|\tilde{F_n}(f)\right| = |A_n| \sqrt{\frac{\left(\frac{1}{\tau_n^2} + 4\pi^2 f^2\right)\cos^2\phi + 4\pi^2 f_n^2 \sin^2\phi - \frac{2\pi f_n}{\tau_n}\sin(2\phi)}{\left[4\pi^2(f_n^2 - f^2) + \frac{1}{\tau_n^2}\right]^2 + 16\pi^2 \frac{f^2}{\tau_n^2}}}. \tag{S4}$$

The latter expression is maximized for the following frequencies:

$$f_{MAX} = \pm \sqrt{\frac{2\pi f_n \sqrt{\frac{4}{\tau_n^2}\cos^2\phi + 4\pi^2 f_n^2 - \frac{4\pi f_n}{\tau_n}\sin(2\phi)} + \frac{2\pi f_n}{\tau_n}\sin(2\phi) - \frac{1}{\tau_n^2}\cos^2\phi - 4\pi^2 f_n^2 \sin^2\phi}{4\pi^2 \cos^2\phi}} \tag{S5}$$

The modulus of the acoustic signal's Fourier's transform (equation S4) displays a complicated expression, which depends on the signal phase ϕ. However, if the oscillation period is much smaller than the decay times, i.e. $f_n \gg 1/\tau_n$, and for frequencies around the breathing

mode frequencies ($|f| \simeq f_n$) a simplification can be introduced.

First of all, $\frac{1}{\tau_n^2}$ is negligible with respect to $4\pi^2 f_n^2$ and hence N, the numerator of the fraction under the square root in expression S4, reduces to:

$$N \approx 4\pi^2 f^2 \cos^2\phi + 4\pi^2 f_n^2 \sin^2\phi - \frac{2\pi f_n}{\tau_n}\sin(2\phi) \approx$$

$$\approx 4\pi^2 f^2 \left(\cos^2\phi + \sin^2\phi\right) - \frac{2\pi f_n}{\tau_n}\sin(2\phi) = 4\pi^2 f^2 - \frac{2\pi f_n}{\tau_n}\sin(2\phi) \approx 4\pi^2 f^2.$$

Now we introduce some approximations also for D, the denominator of the fraction under the square root in equation S4. First of all we drop the term $1/\tau_n^4$ to obtain:

$$D \approx 16\pi^4 (f_n^2 - f^2)^2 + 8\pi^2 \frac{f_n^2 - f^2}{\tau_n^2} + 16\pi^2 \frac{f^2}{\tau_n^2}.$$

Furthermore, if $|f| \simeq f_n$, then we can write $|f| \simeq f_n + \xi$, with $\xi \ll f_n$, and hence $f_n^2 - f^2 = -\xi^2 - 2f_n\xi \approx -2f_n\xi \approx -2|f|\xi = -2|f|(|f| - f_n)$. Considering this approximation we get the following expression:

$$D \approx 64\pi^4 f^2 (|f| - f_n)^2 - 16\pi^2 |f| \frac{|f| - f_n}{\tau_n^2} + 16\pi^2 \frac{f^2}{\tau_n^2} \approx 64\pi^4 f^2 (|f| - f_n)^2 + 16\pi^2 \frac{f^2}{\tau_n^2}.$$

Now substituting the aforementioned approximations for N and D into the expression for $\left|\tilde{F}_n(f)\right|$ to obtain:

$$\left|\tilde{F}_n(f)\right| = |A_n| \sqrt{\frac{N}{D}} \approx |A_n| \sqrt{\frac{4\pi^2 f^2}{64\pi^4 f^2 (|f| - f)^2 + 16\pi^2 \frac{f^2}{\tau_n^2}}} = \frac{|A_n|}{2} \frac{\tau_n}{\sqrt{\left[2\pi\tau_n (|f| - f_n)\right]^2 + 1}}. \tag{S6}$$

Equation S6, which is valid under the limits $f_n \gg 1/\tau_n$ and $|f| \simeq f_n$, does not depend on the phase ϕ and it displays a peak for the frequency $f_{MAX} = \pm f_n$. As a consequence, under these approximations the modulus of the Fourier's transform is independent on the acoustic signal's phase. In Figure S1 a comparison between the non-approximated function

from Equation S4, calculated for the phases $\phi \in \{0, \pi/8, \pi/4, 3\pi/8, \pi/2\}$, is visible. The used values are n=1, f_1=30GHz, τ_1=0.2ns (in agreement with the numbers reported in Figure 3 of the main text), so that $f_1 = 6/\tau_1$, and hence the condition $f_1 >> 1/\tau_1$ is satisfied for the system under investigation. The differences among the functions plotted in Figure S1 are negligible (vertical axis is in logarithmic scale) and, consequently, Equation S6 is a reliable approximation for $|\tilde{F}_n(f)|$.

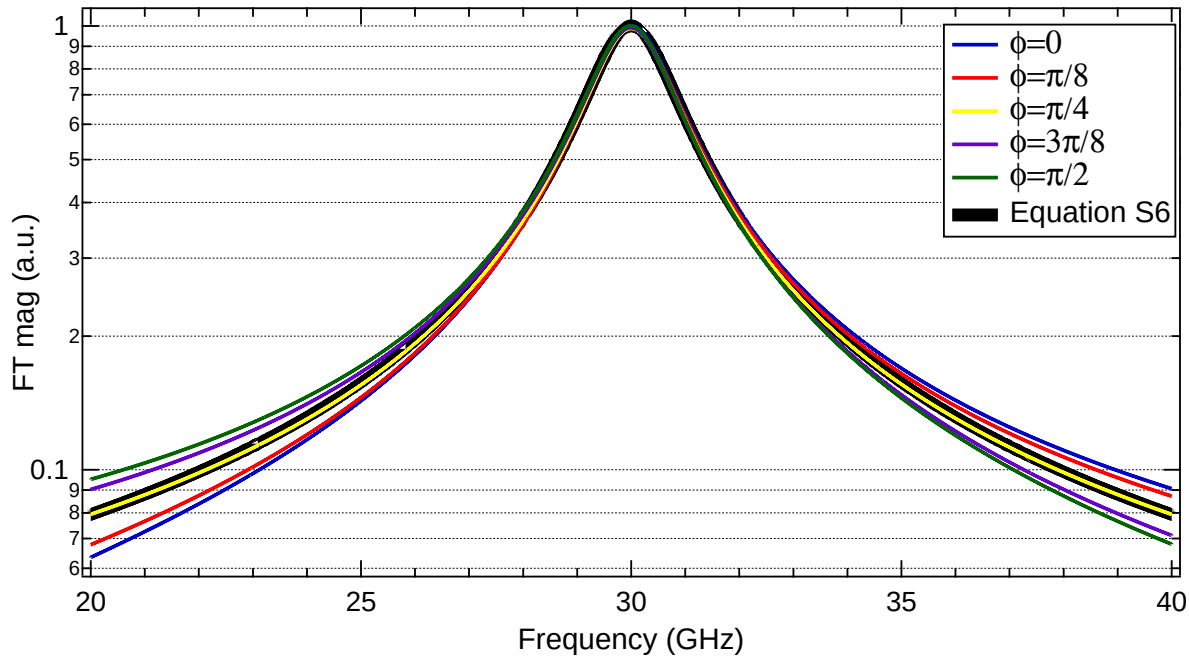

Figure S1: Normalized Fourier's transform magnitude $|\tilde{F}(f)|$ of the photoacoustic signal expected for different initial phases, from eq. S4 and for the approximated equation (S6). The used values are $n = 1$, $f_1 = 30$ GHz, $\tau_1 = 0.2$ ns. The vertical axis is in logarithmic scale to ease its visualization. The peaks' position and FWHM is almost the same for each starting phase ϕ.

2.2 Details of the model: derivation of Eq.s 3 and 4

As we have already described in the main text, the technique excites the longitudinal breathing modes, so the problem can be considered as one-dimensional (1D). Furthermore the Ag NP film, whether fluid-infiltrated or not, is mimicked as a homogeneous isotropic layer of thickness h,[5] characterized by the effective stiffness constant C_{11}^* and density ρ^* (see figure

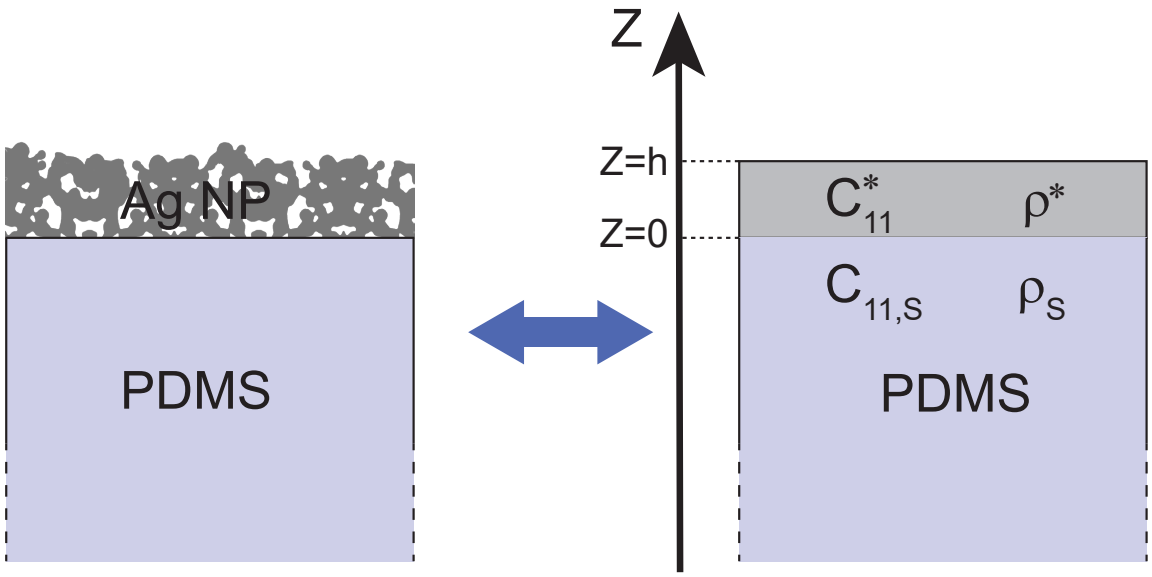

Figure S2: Left: sketch of the Ag porous film on the PDMS substrate. Right: Continuum mechanics model: the Ag NP thin film has been modeled as a homogeneous and isotropic 1D film, characterized by the effective stiffness constant C_{11}^* and density ρ_{11}^*. The film is anchored to a semi-infinite homogeneous and isotropic PDMS substrate of stiffness constant $C_{11,S}$ and density ρ_S.

S2). The film is anchored to a semi-infinite homogeneous and isotropic PDMS substrate with stiffness constant $C_{11,S}$ and density ρ_S. Referring to the coordinate system reported in Figure S2, the longitudinal displacement field component $u_z(z,t)$ satisfies the wave equation

$$\frac{\partial^2 u_z(z,t)}{\partial t^2} = v_j^2 \frac{\partial^2 u_z(z,t)}{\partial z^2} \tag{S7}$$

where z is the direction perpendicular to the film surface, the subscript j=$\{NP, S\}$ identifies the NPs film and PDMS substrate respectively, v_{NP}=$\sqrt{C_{11}^*/\rho^*}$ and v_S=$\sqrt{C_{11,S}/\rho_S}$ are the longitudinal wave velocities in the NP film and in the PDMS substrate, respectively.

The equation is separable and the solution can be written in the form $u_z(z,t)$=$U(z)T(t)$. We search for solutions of the type $U(z)$=$u_{k_j}\exp(ik_jz)$+$u_{-k_j}\exp(\text{-}ik_jz)$ and $T(t)$=$u_\omega\exp(\text{-}i\omega t)$, resulting in the dispersion relation ω^2=$v_j^2k_j^2$ with ω and k_j the angular frequency and the wave vector in material j respectively.

We assign a stress free (Equation S8) boundary condition on the film surface (z=h), while

the interface (z=0) between the PDMS (z<0) and the NP film (z>0) is assumed as "perfect". The latter condition is formally defined requiring continuity of displacement (Equation S9) and stress (equivalent to Equation S10) at the junction of the two media:

$$\left.\frac{\partial U}{\partial z}\right|_{z=h} = 0 \tag{S8}$$

$$U(0-) = U(0+) \tag{S9}$$

$$C_{11,S}\left.\frac{\partial U}{\partial z}\right|_{0-} = C_{11}^{*}\left.\frac{\partial U}{\partial z}\right|_{0+} \tag{S10}$$

The PDMS substrate is taken as semi-infinite. For this reason the plane wave solution propagating from the substrate toward the interface - regressive solution - is set to zero, resulting in $U(z)$=u_{-k_s}exp(-jk_sz) for z<0. Forcing $U(z)$ to satisfy the above-mentioned boundary conditions, and accounting for the fact that $Z > Z_S$, we obtain a dispersion relation allowing for complex solutions ω_n=$Re\{\omega_n\}$+$iIm\{\omega_n\}$ only:

$$Re\{\omega_n\} = \pi\frac{v_{NP}}{h}n \tag{S11}$$

$$Im\{\omega_n\} = \frac{v_{NP}}{2h}\ln\left(\frac{Z - Z_S}{Z + Z_S}\right) \tag{S12}$$

where Z=$\sqrt{C_{11}^{*}\rho^{*}}$ and Z_S=$\sqrt{C_{11,S}\rho_S}$ are the acoustic impedance of the film and of the substrate respectively, while n=$\{1, 2, 3...\}$.

It is worth mentioning that $Im\{\omega_n\}$<0 and it does not depend on the mode index n. We obtain a complex angular frequency since the regressive propagating wave in the substrate has been forcibly avoided, leaving the elastic wave radiated from the NP film to the substrate as the only possible solution within the substrate. The acoustic problem is thus energetically open and the solutions are promoted to quasi-stationary states, the film's breathing modes being exponentially damped harmonic oscillations.

From equations S11 and S12 it is possible to obtain the expressions for breathing mode

frequency and dacay time, as described in equations S13 and S14

$$f_n = \frac{Re\{\omega_n\}}{2\pi} = \frac{v_{NP}}{2h} n = f_1 n, \tag{S13}$$

$$\tau_n = \frac{1}{|Im\{\omega_n\}|} = \left| f_1 \ln\left(\frac{Z - Z_S}{Z + Z_S}\right)\right|^{-1} \tag{S14}$$

which correspond to equation 3 and 4 of the main text.

2.3 A possible mechanism to convey water to the device

The description of the mechanisms to convey water to the device is beyond the scopes of the present paper. Nevertheless we here suggest a possible route (one among many) to achieve an homogeneous filling of the porous film avoiding a superficial thick water layer and air clogging of the scaffold channels. The device may be homogeneously water infiltrated by means of the surface adsorbed water layer due to moisture. It has been shown that it is possible to tune the thickness of the water adsorbed layer on a flat SiO_2 wafer from 0 to 3 nm just by varying the relative humidity.[6] Considering that the contact angles for SiO_2 and metallic Ag are similar,[7,8] especially in humid environment,[9] we expect a similar wetting of the scaffold here proposed. Furthermore, the nano-granular nature of the scaffold does not strongly affect its surface energy.[10]

3 The Practical Case

3.1 Materials constants

Here we report the literature values for bulk Ag, water and PDMS, together with the computed effective elastic constants and acoustic impedances for the infiltrated porous film described in the main text.

The film constituents normalised concentrations are:

- $c_{Ag} = FF \approx 64\%$
- $c_{water} = (1 - FF)\, l$
- $c_{voids} = (1 - FF)\,(1 - l)$

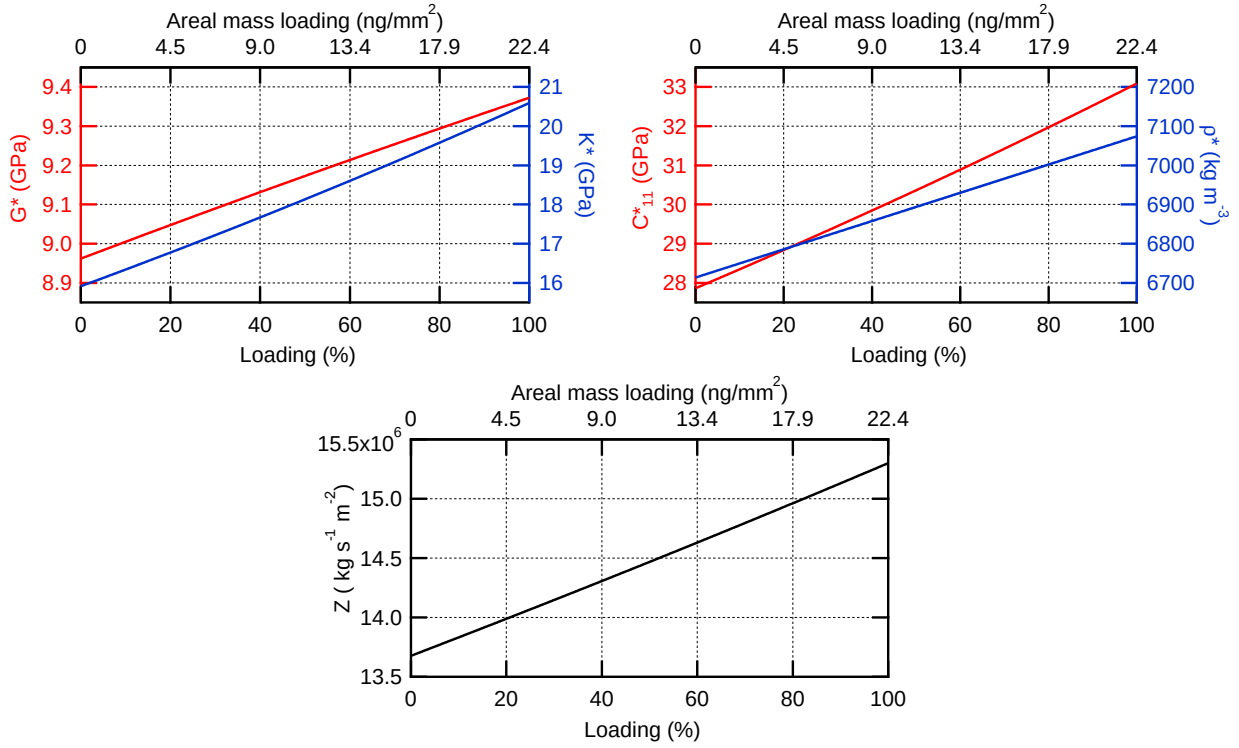

Figure S3: Computed values for the porous film as a function of the water loading. Top-left: shear (G^*, red line) and bulk (K^*, blue line) effective moduli. Top-right: effective C^*_{11} (red line) and density (ρ^*, blue line). These values are retrieved by using the Budiansky method.[11] Bottom: effective acoustic impedance $Z{=}\sqrt{C^*_{11}\rho^*}$.

In Table S1 the elastic constants (K and G) for the used materials are reported together with references from the literature.

Figure S3 shows the computed elastic constants and acoustic impedance for the porous film as a function of the water loading l.

Table S1: Summary of the mechanical properties adopted in this article.

K_{Ag}	100	GPa	[5]
G_{Ag}	30	GPa	[5]
ρ_{Ag}	10490	kg/m^3	[12]
K_w	2.2	GPa	[13]
G_w	0		
ρ_w	1000	kg/m^3	[14]
v_s	1290	m/s	[15]
ρ_s	965	kg/m^3	[16]
Z_s	1.2×10^6	kg s^{-1} m^{-2}	$v_s * \rho_s$

3.2 Layered cases for n≤3

We report the device loading curves for the first three breathing modes both for the cases of homogeneous and layered filling. These include Figure 4 of the main manuscript.

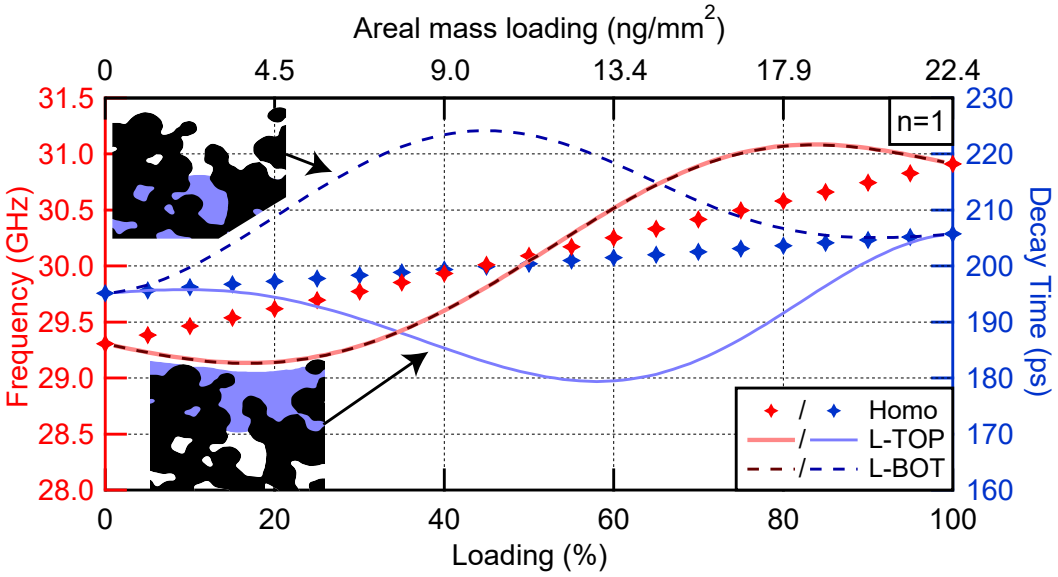

Figure S4: Frequency of the n=1 acoustic breathing modes (left axis, red) and decay times (right axis, blue) vs water filling within the layered adsorption scenarios L-TOP (full lines), L-BOT (dashed lines) and, for sake of comparison, for the homogeneous wetting case (markers). Water filling is expressed both as relative volumetric loading l (bottom axis) and equivalent areal mass loading m_s (top axis). Cartoon: schematics of the infiltrated device for the L-TOP (bottom cartoon) and L-BOT (top cartoon) scenarios. Water is depicted in blue.

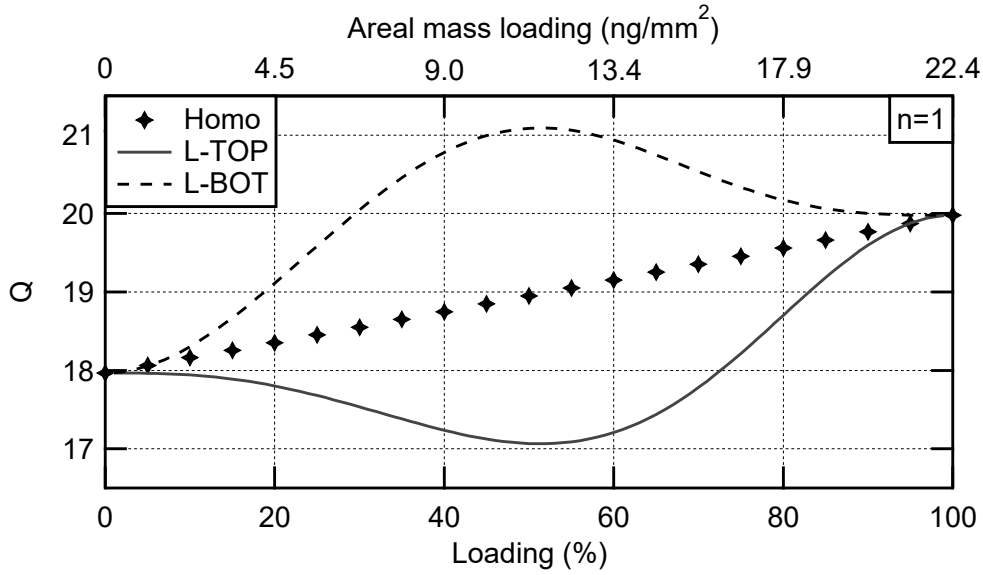

Figure S5: Quality factor of the n=1 acoustic breathing modes vs water filling within the homogeneous and the layered adsorption scenarios L-TOP (full lines), L-BOT (dashed lines). Water filling is expressed both as relative volumetric loading l (bottom axis) and equivalent areal mass loading m_s (top axis).

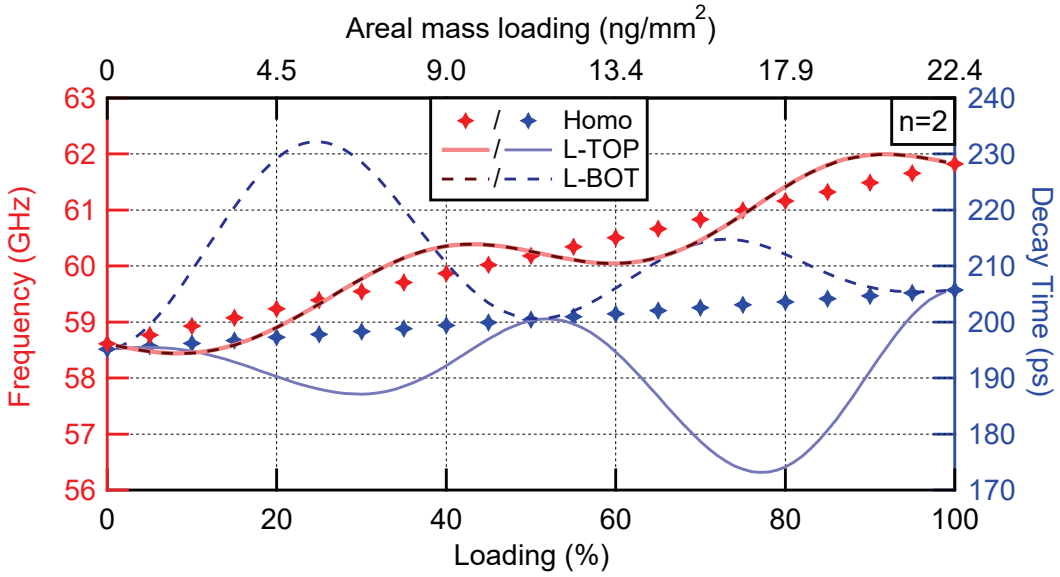

Figure S6: Frequency of the n=2 acoustic breathing modes (left axis, red) and decay times (right axis, blue) vs water filling within the layered adsorption scenarios L-TOP (full lines), L-BOT (dashed lines) and, for sake of comparison, for the homogeneous wetting case (markers). Water filling is expressed both as relative volumetric loading l (bottom axis) and equivalent areal mass loading m_s (top axis).

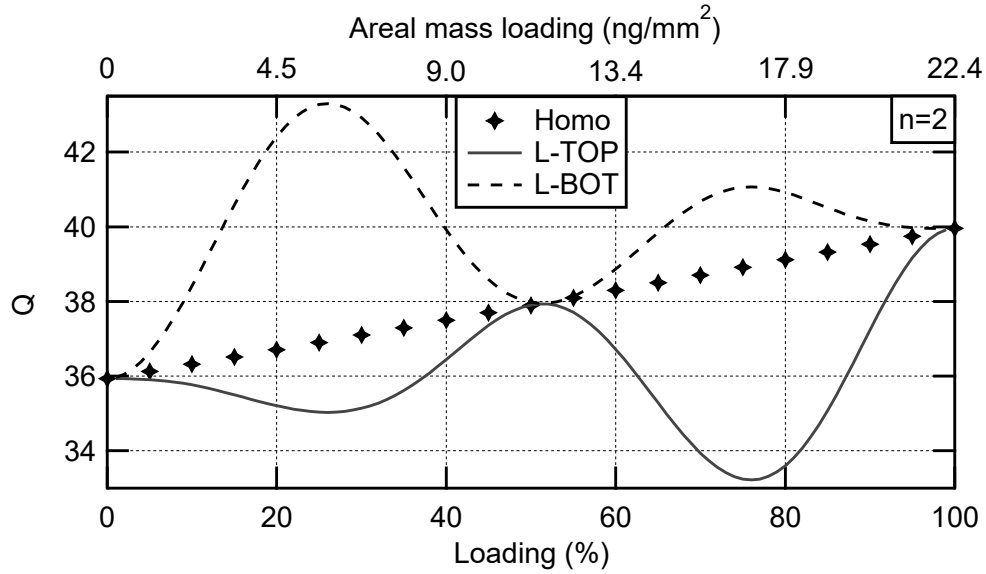

Figure S7: Quality factor of the n=2 acoustic breathing modes vs water filling within the homogeneous and the layered adsorption scenarios L-TOP (full lines), L-BOT (dashed lines). Water filling is expressed both as relative volumetric loading l (bottom axis) and equivalent areal mass loading m_s (top axis).

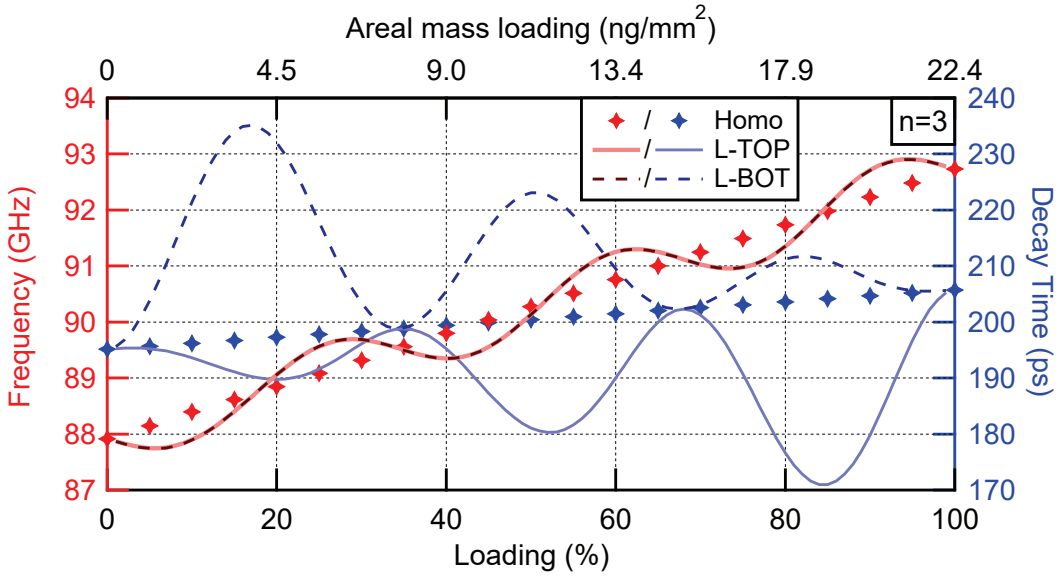

Figure S8: Frequency of the n=3 acoustic breathing modes (left axis, red) and decay times (right axis, blue) vs water filling within the layered adsorption scenarios L-TOP (full lines), L-BOT (dashed lines) and, for sake of comparison, for the homogeneous wetting case (markers). Water filling is expressed both as relative volumetric loading l (bottom axis) and equivalent areal mass loading m_s (top axis).

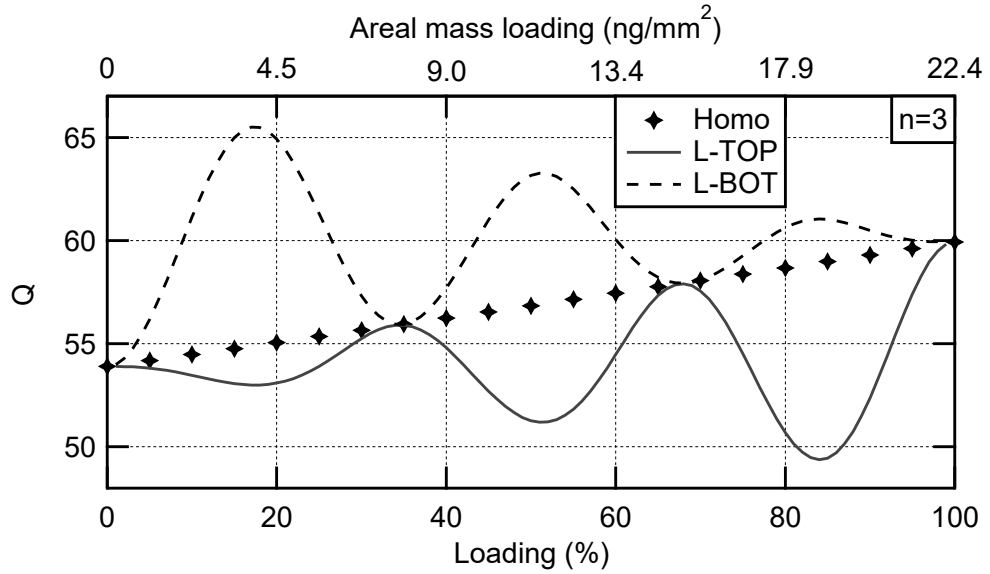

Figure S9: Quality factor of the n=3 acoustic breathing modes vs water filling within the homogeneous and the layered adsorption scenarios L-TOP (full lines), L-BOT (dashed lines).Water filling is expressed both as relative volumetric loading l (bottom axis) and equivalent areal mass loading m_s (top axis).

References

(1) Benetti, G.; Caddeo, C.; Melis, C.; Ferrini, G.; Giannetti, C.; Winckelmans, N.; Bals, S.; Van Bael, M. J.; Cavaliere, E.; Gavioli, L.; Banfi, F. Bottom-Up Mechanical Nanometrology of Granular Ag Nanoparticles Thin Films. *J. Phys. Chem. C* **2017**, *121*, 22434–22441.

(2) Saito, T.; Toriwaki, J.-I. New Algorithms for Euclidean Distance Transformation of an N-Dimensional Digitized Picture With Applications. *Pattern Recognit.* **1994**, *27*, 1551 – 1565.

(3) Hildebrand, T.; Rüegsegger, P. A New Method for the Model-Independent Assessment of Thickness in Three-Dimensional Images. *J. Microsc.* **1997**, *185*, 67–75.

(4) Doube, M.; Kłosowski, M. M.; Arganda-Carreras, I.; Cordelières, F. P.; Dougherty, R. P.; Jackson, J. S.; Schmid, B.; Hutchinson, J. R.; Shefelbine, S. J. BoneJ: Free and extensible bone image analysis in ImageJ. *Bone* **2010**, *47*, 1076–1079.

(5) Peli, S.; Cavaliere, E.; Benetti, G.; Gandolfi, M.; Chiodi, M.; Cancellieri, C.; Giannetti, C.; Ferrini, G.; Gavioli, L.; Banfi, F. Mechanical Properties of Ag Nanoparticle Thin Films Synthesized by Supersonic Cluster Beam Deposition. *J. Phys. Chem. C* **2016**, *120*, 4673–4681.

(6) Asay, D. B.; Kim, S. H. Evolution of the Adsorbed Water Layer Structure on Silicon Oxide at Room Temperature. *J. Phys. Chem. B* **2005**, *109*, 16760–16763.

(7) Bartell, F. E.; Cardwell, P. H. Reproducible Contact Angles on Reproducible Metal Surfaces. I. Contact Angles of Water against Silver and Gold1. *J. Am. Chem. Soc.* **1942**, *64*, 494–497.

(8) Holysz, L.; Miroslaw, M.; Terpilowski, K.; Szczes, A. Influence of Relative Humidity on the Wettability of Silicon Wafer Surfaces. *Annales UMCS, Chemistry* **2008**, *63*.

(9) Bartell, F. E.; Smith, J. T. Alteration of Surface Properties of Gold and Silver as Indicated by Contact Angle Measurements. *J. Phys. Chem.* **1953**, *57*, 165–172.

(10) Aqra, F.; Ayyad, A. Surface Free Energy of Alkali and Transition Metal Nanoparticles. *Appl. Surf. Sci.* **2014**, *314*, 308–313.

(11) Budiansky, B. On the Elastic Moduli of Some Heterogeneous Materials. *J. Mech. Phys. Solids* **1965**, *13*, 223–227.

(12) Auld, B. A. *Acoustic Fields and Waves in Solids, Vol 1*; John Wiley and Sons, 1973.

(13) Halliday, D.; Resnick, R.; Walker, J. *Fundamentals of Physics.*; Wiley: New York, 1997; OCLC: 35746861.

(14) WEAST, R. C. *Handbook of Chemistry and Physics*; Chemical Rubber Company, 1969.

(15) Travagliati, M.; Nardi, D.; Giannetti, C.; Gusev, V.; Pingue, P.; Piazza, V.; Ferrini, G.; Banfi, F. Interface Nano-Confined Acoustic Waves in Polymeric Surface Phononic Crystals. *Appl. Phys. Lett.* **2015**, *106*, 021906.

(16) Mark, J. E. Polymer Data Handbook: Oxford University Press. *New York* **1999**,